Lithologic variation within bright material on Vesta revealed by linear spectral unmixing

CrossMark

F. Zambon [a,*], F. Tosi [a], C. Carli [a], M.C. De Sanctis [a], D.T. Blewett [b], E. Palomba [a],
A. Longobardo [a], A. Frigeri [a], E. Ammannito [c], C.T. Russell [c], C.A. Raymond [d]

[a] INAF-IAPS Istituto di Astrofisica e Planetologia Spaziali, Via del Fosso del Cavaliere, 100, 00133 Rome, Italy
[b] Johns Hopkins University Applied Physics Laboratory, Laurel, MD 20723, USA
[c] Institute of Geophysics and Planetary Physics, University of California at Los Angeles, 3845 Slichter Hall, 603 Charles E. Young Drive, East, Los Angeles, CA 90095-1567, USA
[d] NASA/Jet Propulsion Laboratory and California Institute of Technology, 4800 Oak Grove Drive, Pasadena, CA 91109, USA

ABSTRACT

Vesta's surface is mostly composed of pyroxene-rich lithologies compatible with howardite, eucrite and diogenite (HED) meteorites (e.g., McCord et al. [1970] Science, 168, 1445–1447; Feierberg & Drake [1980] Science, 209, 805–807). Data provided by the Visible and Infrared (VIR) spectrometer, onboard the NASA Dawn spacecraft, revealed that all Vesta reflectance spectra show absorption bands at ∼0.9 and ∼1.9 μm, which are typical of iron-bearing pyroxenes (De Sanctis et al. [2012] Science, 336, 697–700). Other minerals may be present in spectrally significant concentrations; these include olivine and opaque phases like those found in carbonaceous chondrites. These additional components modify the dominant pyroxene absorptions. We apply linear spectral unmixing on bright material (BM) units of Vesta to identify HEDs and non-HED phases. We explore the limits of applicability of linear spectral unmixing, testing it on laboratory mixtures. We find that the linear method is applicable at the VIR pixel resolution and it is useful when the surface is composed of pyroxene-rich lithologies containing moderate quantities of carbonaceous chondrite, olivine, and plagioclase. We found three main groups of BM units: eucrite-rich, diogenite-rich, and olivine-rich. For the non-HED spectral endmember, we choose either olivine or a featureless component. Our work confirms that Vesta's surface contains a high content of pyroxenes mixed with a lower concentration of other phases. In many cases, the non-HED endmember that gives the best fit is the featureless phase, which causes a reduction in the strength of both bands. The anticorrelation between albedo and featureless endmember indicates that this phase is associated with low-albedo, CC-like opaque material. Large amounts of olivine have been detected in Bellicia, Arruntia and BU14 BM units. Other sites present low olivine content (<30%) mostly with a high concentration of diogenite.

1. Introduction

1.1. Early knowledge of Vesta

The first spectral study of Vesta dates back to Bobrovnikoff (1929). McCord et al. (1970) compared Vesta spectra with the meteorite Nuevo Laredo, inferring a relation between Vesta and pyroxenes. Pyroxenes are characterized by the presence of two crystal field absorptions, centered approximately at 0.9 and 1.9 μm (McCord et al., 1970), due to ferrous iron (Fe^{2+}) in octahedral sites (e.g., Burns, 1993). Consolmagno and Drake (1977)

suggested a possible link between Vesta and eucrite meteorites, and Feierberg and Drake (1980) proposed that Vesta is a mixture of howardite and eucrite. Studies by Lupishko et al. (1988) show a clear inverse correlation between the polarization and brightness of Vesta, correlated with the west–east dichotomy. Hubble Space Telescope (HST) observations between 1994 and 1996 confirmed this inference by highlighting the geological differences on the asteroid (Binzel et al., 1997). Moreover the identification of the prominent impact basin at the south pole (now named Rheasilvia) corroborates the hypothesis that Vesta is the parent body of the howardite, eucrite and diogenite (HED) meteorites (Thomas et al., 1997). In addition, the disk-integrated mid-infrared spectra of Vesta have shown the presence of minor constituents as olivine, feldspar, and chromite (Donaldson Hanna and Sprague, 2009). Studies by Li et al. (2010) revealed that the vestan surface can be

* Corresponding author: Tel.: +39 06 45488210, +39 06 49934210; fax: +39 06 45488188.

E-mail address: francesca.zambon@iaps.inaf.it (F. Zambon).

divided into several geological units (more specifically, regions of lithologic variation), in particular, eucrite-rich and diogenite-rich units, as well as slightly weathered and freshly exposed units. Shestopalov et al. (2010) concluded that the global diversity of Vesta might be caused by variations of non-basaltic source sediments enriched by dark rocks, spinel group minerals, or even chondritic-like material. Moreover, they showed that certain vestan units contain olivine abundances of several volume percent.

1.2. The Dawn era and Vesta's lithologies

Dawn entered orbit around Vesta in July 2011 (Russell and Raymond, 2011), and enabled many discoveries during about one year of observations. For the first time, Dawn acquired data of Vesta's surface at high spatial resolution, allowing for production of complete geological and lithological maps (De Sanctis et al., 2012a; Williams et al., 2014). Dawn's Visible and Infrared (VIR) imaging spectrometer (De Sanctis et al., 2011) provided high spectral resolution data covering the majority of Vesta's surface at varying spatial scales. The spatial resolution of the VIR maps ranges from ∼800 m/pixel in the Survey phase to ∼180 m/pixel in the HAMO and HAMO-2 phases (see Table 1 of Zambon et al. (2015)).

Vesta is the parent body of the HED meteorites. HEDs encompass a large variety of igneous rocks, similar to basalts, cumulate gabbros, orthopyroxenites and igneous brecciated mixtures (Mittlefehldt et al., 1998). Diogenites are coarse-grained cumulates that originated in a plutonic layer deep in the crust (Beck and McSween, 2010; McSween et al., 2013, 2011; Mittlefehldt et al., 1998). The mineralogy of diogenites is dominated by orthopyroxenes (from 87% to 99%); all diogenites contain < 5% chromite and some contain olivine, typically at contents < 10% (McSween et al., 2011). Eucrites occur as basaltic or cumulate rocks. They are dominated by Ca-poor pyroxenes and plagioclase, with minor amounts of metal, troilite, chromite, ilmenite, and silica (Mayne et al., 2010; McSween et al., 2011). Eucrites are believed to have crystallized as lavas on the surface or within relatively shallow dikes and plutons (McSween et al., 2011). Basaltic eucrites contain Fe-rich pyroxenes, whereas cumulate eucrites are predominantly unbrecciated and their chemistry is similar to basaltic eucrites, but richer in Mg (McSween et al., 2011; Mittlefehldt et al., 1998). Howardites are brecciated achondrites, principally mixtures of eucrite and diogenite clasts, and reflectance spectra of howardites have pyroxene band center positions intermediate between those of eucrites and diogenites (McSween et al., 2011; Mittlefehldt et al., 1998). Impact mixing of eucrite and diogenite has produced the polymict breccias and howardites.

Eucrite, diogenite and howardite lithologies are present on Vesta's surface, as revealed by VIR data (Ammannito et al., 2013a; De Sanctis et al., 2012a) augmented by Dawn Framing Camera images (Reddy et al., 2012b) and Gamma Ray And Neutron Detector data (Lawrence et al., 2013; Prettyman et al., 2014, 2011, 2013). Recently, many papers on the analysis of Vesta's surface composition using Dawn data have been published (e.g., Ammannito et al., 2013a; De Sanctis et al., 2013b; Ruesch et al., 2014; Le Corre et al., 2013; Reddy et al., 2013; Thangjam et al., 2013). The crust of Vesta is dominated by howardite enriched in eucrite (De Sanctis et al., 2012a; 2013b). A few outcrops of diogenite are present in localized areas in the south polar region, corresponding to the rim of the large impact basin Rheasilvia. Large areas of diogenite-enriched howardite have also been identified in the northern hemisphere (longitude 0°–90°E) and are interpreted to consist of Rheasilvia ejecta (Ammannito et al., 2013a; De Sanctis et al., 2012a).

Ammannito et al. (2013a) suggested a high content of olivine (50–80 vol.%) in the area of Bellicia (lat 40°N, lon 40°E) and Arruntia craters (lat 40°N, lon 70°E), highlighting the presence of lithologies different from that of typical HEDs. Others 11 sites containing much smaller amounts of olivine (located up to 39°S latitude) have also been identified by Ruesch et al. (2014), and six other new olivine-rich regions were proposed by Palomba et al. (2015), almost all located at latitudes below 28°N. Dark material units on Vesta were discussed by Jaumann et al. (2012), McCord et al. (2012), Reddy et al. (2012a), and Palomba et al. (2014). Hydrated mineral phases were shown to be correlated with this low-reflectance material (De Sanctis et al., 2012b), confirming that the dark material can be attributed to the presence of a carbonaceous chondrite (CC)-like component delivered by impacts.

1.3. Bright material units: A slice of fresh material

The spectral analysis of the bright material units reveals that they are generally characterized by greater band depths than their surroundings. Most bright units have a howardite rich-eucrite, composition, with some exceptions such as the bright unit called "BU15" in Zambon et al. (2014).

BM units could represent pristine material that has been recently exposed on the surface, and thus contains less carbonaceous-chondrite-like contamination introduced by impact mixing than other areas of Vesta (see Zambon et al., 2014 for more detail). To be consistent with Zambon et al. (2014), we follow the same classification of the BM units, as described by Mittlefehldt et al. (2012). The abbreviation CWM stands for crater wall material, SM means slope material, and RM refers to radial material. The spectral analysis employed in Zambon et al. (2014) to derive Vesta's lithologies is based on selected spectral parameters, namely band center (BC), band depth (BD) and band area ratio (BAR).

The goal of our work is to use linear spectral unmixing to automatically identify the main lithologies of specific regions and determine their semi-quantitative mixing coefficients, including identification and mapping of mineralogical phases other than the spectrally dominant pyroxenes. The mixing coefficients depend on various effects, such as, the grain size, the abundance of the mineralogical phases present in the scene, and the scale at which the components are mixed (i.e., macroscopic vs. intimate; Combe et al., 2008). Since the grain size on Vesta, at the VIR spatial scale, is quite homogeneous ($< 25-45$ μm) (Hiroi et al., 1994; Palomba et al., 2014; Zambon et al., 2014), we can assume that the grain size does not substantially affect our derived mixing coefficients. Thus the unmixing results principally depend on the abundance of the mineralogical phases and on the type of mixing.

Unmixing methods are useful for understanding the composition of a surface (e.g. Bioucas-Dias et al., 2012; Keshava and Mustard, 2002; Pieters and Englert, 1993). Mixing models can be either linear or non-linear. In the linear case, the spectrum of a region can be considered the area-weighted average of the endmembers present (Bioucas-Dias et al., 2012; Hapke, 2012; Singer and McCord, 1979). The endmembers can be extracted from the scene, or can be reference spectra of plausible analogue phases. The endmembers are generally assumed to represent the different components, which are the fundamental constituents of the scene, so that each pixel in the scene can be modeled as a linear combination of the endmembers (Bioucas-Dias et al., 2012).

The case of non-linear mixing arises when light is scattered by multiple materials in the scene. Scattered light interacts with more than one endmember, and the resulting spectrum is a non-linear combination of the components. Models for non-linear mixing require comprehensive information on the expected minerals, such as scattering coefficients, particle sizes, and optical constants (e.g., Hapke, 1981; Shkuratov et al., 1999). Here we use linear unmixing as a first step in order to derive additional information on the composition of Vesta's surface.

The linear unmixing approach was widely used in the past to model spectroscopic data of a variety of bodies (e.g., Adams et al., 1986; Blewett et al., 1995; Combe et al., 2008; Dalton, 2007; Fox III et al., 1990; McCord et al., 2012; Ramsey and Christensen, 1992). Adams et al. (1986) already applied linear unmixing methods to Viking lander data of Mars, while Dalton (2007) applied linear unmixing to Europa data using a set of laboratory spectra as endmembers, and Combe et al. (2008) used the Multiple-Endmember Linear Spectral Unmixing Model (MELSUM) to analyze Mars data from the Infrared Mineralogical Mapping Spectrometer (OMEGA) onboard MarsExpress. A first use of linear unmixing methods on Vesta was presented by McCord et al. (2012), who found that the entire surface of Vesta as observed by VIR could be modeled using the weighted sum spectral endmembers, 'bright' and 'dark' (McCord et al., 2012). In this paper, we apply the same linear unmixing method employed by Tosi et al. (2015) and Zambon et al. (2015) to extended areas of Vesta.

Here we considered high spatial resolution data from the Dawn mission at Vesta, and we selected a set of plausible laboratory spectra analogues as endmembers. We apply the linear unmixing method to the bright material (BM) units of Vesta, previously analyzed by Zambon et al. (2014). BM units are often associated with impact craters. Impacts expose fresh, unweathered material from beneath the surface, which could be indicative of the original vestan crust composition (Zambon et al., 2014). The previous spectral analysis revealed the main lithologies (eucrite, diogenite and howardite) and the spectral characteristics of these units. Here we study the same BM units with the goal of quantifying the mixing coefficients of the different lithologies. We also aim to identify the presence of other mineralogical phases in addition to the spectrally dominant, HED components. In principle, this work can be extended also to broader regions on Vesta, with the main goal of determining the global distribution of Vesta's non-HED lithologies.

2. Dataset description and VIR spectra characteristics

The Dawn mission at Vesta consisted of four phases, based on the altitude of the spacecraft: Survey (2735 km altitude), HAMO (High Altitude Mapping Orbit, 695 km), LAMO (Low Altitude Mapping Orbit, 210 km) and HAMO-2, an extension of the mission similar to the HAMO phase (Russell and Raymond, 2011). Here we used HAMO and HAMO-2 VIR data, which cover large part of Vesta's surface with a high spatial resolution (∼180 m/pixel). The VIR instrument has two distinct detectors, or "channels": the visible, covering wavelengths from 0.25 to 1.07 μm, and the infrared, with sensitivity from 1.02 to 5.10 μm (De Sanctis et al., 2011). Each channel has 432 spectral bands, so the average spectral sampling is 1.8 nm/band for the visible channel and 9.8 nm/band for the infrared channel (De Sanctis et al., 2011). Each VIR image cube has 256 spatial samples with a variable number of lines determined by the length of a scan, and 432 spectral bands.

For details about the VIR data calibration, refer to a document archived at the NASA Planetary Data System Small Bodies Node: http://sbn.psi.edu/archive/dawn/vir/DWNVVIR_I1B/DOCUMENT/ VIR_CALIBRATION/VIR_CALIBRATION_V2_4.PDF. The VIR visible and infrared data are each separately geo-referenced, then the two VIS and IR subsets are merged together to form a single spectrum covering the entire spectral range from 0.25 to 5.10 μm. The last 19 spectral channels of the visible range, which usually are affected by higher instrumental noise, are discarded.

We use VIR data calibrated in units of reflectance factor (I/F) from 0.6 to 2.5 μm, focusing our analysis on the two pyroxene bands. We consider the average spectra of BM units used for spectral characterization by Zambon et al. (2014). The wavelength position of the centers of the two bands gives information on the HED lithologies. The displacement of the pyroxene band centers is sensitive to temperature variations (e.g., Burbine et al., 2009; Reddy et al., 2012c). However, given the usual range of daytime temperatures recorded on Vesta for BM units (between 252 and 265 K; Tosi et al., 2014), this effect is essentially negligible in VIR data (Longobardo et al., 2014).

The strength (depth) of the pyroxene absorption bands is a function of the abundances of the minerals, the particle size, and the presence of opaque phases (e.g., Clark, 1999). Band depths are also affected by temperature variations and the phase angle of the observations (Longobardo et al., 2014; Reddy et al., 2012c). The relatively small range of temperatures found on Vesta does not affect the band depth shape: Dalton et al. (2011) demonstrated that a temperature range of 150 K is necessary to observe substantial band-depth effects (whereas on Vesta we found variations never larger than 50 K). Band depths are the only spectral parameter among those considered that vary depending on illumination and viewing geometry. However, the variation of band depth with phase angle is very small for bright regions, although variation can become important as albedo decreases (Longobardo et al., 2014). We consider observations at phase angles between 28° and 52° and incidence angles lower than 60° have been selected. According to Longobardo et al. (2014), in this narrow range band depths are only weakly dependent on phase and hence a photometric correction is not mandatory. Phase, incidence and emission angles of the BM units are reported in Tables 7–9 of the Zambon et al. (2014) supplementary online material (SOM).

Here we utilize the "Claudia" coordinate system (Supplemental material of Li et al., 2012; Roatsch et al., 2012; Russell et al., 2012; Reddy et al., 2013), which has been used by Zambon et al. (2014) for tabulation of the BM unit locations.
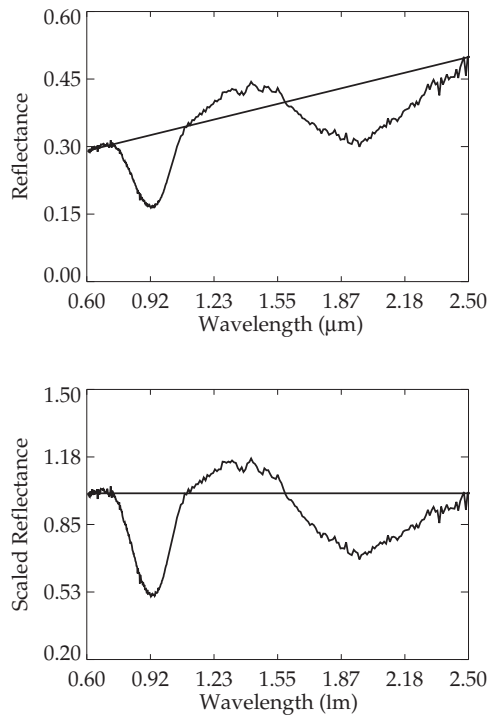
3. Analytical method

3.1. Linear unmixing

Understanding the composition of a surface using reflectance spectroscopy may be challenging. Analysis of spectral parameters is useful but does not offer a complete characterization of the surface materials. Key additional information can be provided by the application of mixing model algorithms. Based on past analysis (Ammannito et al., 2013a; De Sanctis et al., 2012a; 2013a; Jaumann et al., 2012; McCord et al., 2012), we assume that reflectance spectra of Vesta can be reproduced by a linear combination of at least three endmembers, chosen from a sample of eucrites, diogenites, olivines and a featureless endmember. To describe the primary components of Vesta's surface, we consider only diogenite and eucrite endmembers, and do not include howardite as a separate endmember. Howardites, which are the major component of Vesta terrains (De Sanctis et al., 2012a), are brecciated rocks with variable amounts of both eucrite and diogenite; thus howardites can be spectrally characterized by a mixing of the two components. The mixing equation is:

$$Y_{\text{mix}} = a_1 y_1 + a_2 y_2 + a_3 y_3 \tag{1}$$

where y_1, y_2, y_3 are the scaled spectra of the endmembers and a_1, a_2, a_3 are their respective mixing coefficients. The unmixing algorithm requires all mixing coefficients to be non-negative, and their sum must be equal to unity.

The method we developed is able to automatically find the endmembers and the mixing coefficients, subject to the positivity constraint, which allows exclusion of solutions that are not physically meaningful. We outline the principal steps of our algorithm as follows:

1. Spectral slope removal. Normalization of the spectrum by the continuum slope is done for two reasons. First, the position of
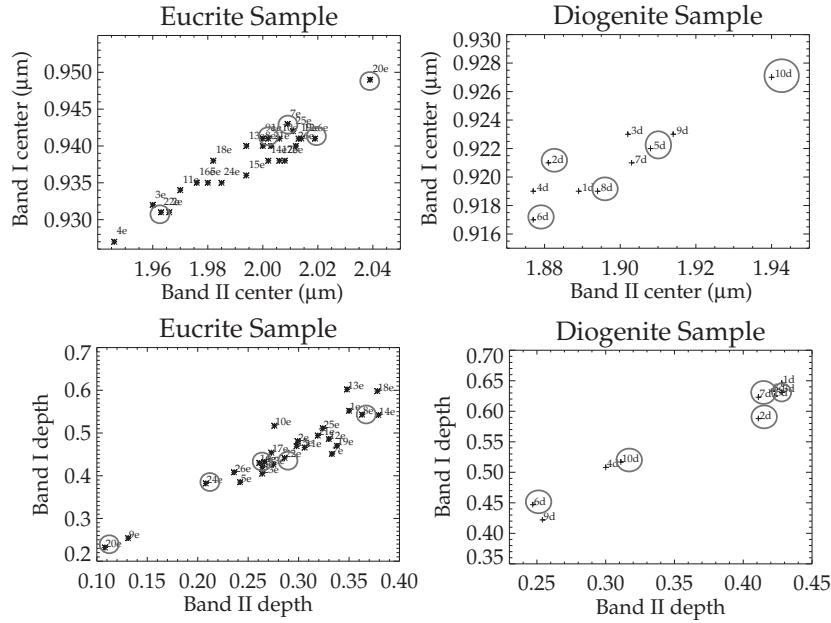
and diogenite. Studies based on the analysis of HED laboratory samples show that the grain size of diogenites in howardite breccias ranges from 500 μm to 1.5 mm whereas the average grain size of eucritic material is $\leq$ 70 μm (Beck et al., 2011; Reddy et al., 2012b; SOM). Previous works based on ground-based observation and remote sensing data suggest that for the spatial resolution available, most of Vesta's surface can be best represented by regolith with particle sizes $<$ 25μm (Hiroi et al., 1994; Palomba et al., 2014; Zambon et al., 2014). This limits our choice to laboratory spectra acquired for samples in the $<$ 25μm size fraction, if available. Since we are working with continuum-removed spectra, absolute reflectance does not enter in our analysis. Therefore, we cannot distinguish between a low-reflectance featureless phase and a high-reflectance featureless phase: we can just observe a decrease in band depth. To account for this effect, we introduce a featureless endmember represented by a straight horizontal line. Nonetheless, examination of the mean albedo values derived in Zambon et al. (2014) for all the bright units can be useful in identifying the presence of low- vs. high-reflectance featureless endmembers.

We selected 14 endmember spectra including six eucrite, five diogenite and two olivine samples from the RELAB database, plus the straight line representing a featureless endmember. This limit is imposed in order to allow computations to be completed in reasonable time. Since eucrite-rich howardite is the dominant component on Vesta's surface (De Sanctis et al., 2013b) and because eucrites show a wide range of petrographic and spectral characteristics, we include a larger number of them in our endmembers set. The endmembers selection was done by considering the spectral parameters, the spectral shape and their petrographic differences. We selected spectra with band centers and band depths that cover the possible range of values (Fig. 2), and those with different spectral characteristics, to take into account all of the possible spectral variations (see Fig. 3). Moreover for eucrite we considered both cumulate and basaltic samples, as well as polymict and monomict material. We also tested the distribution frequency of each spectrum from a preliminary combination of two endmembers chosen among the whole available spectral library, performing a linear unmixing test. With just two endmembers, the entire library of laboratory spectra can be used in the analysis because of the reduced computational time. We calculate the spectral parameters with the same methods described in Section 4 of Zambon et al. (2014).
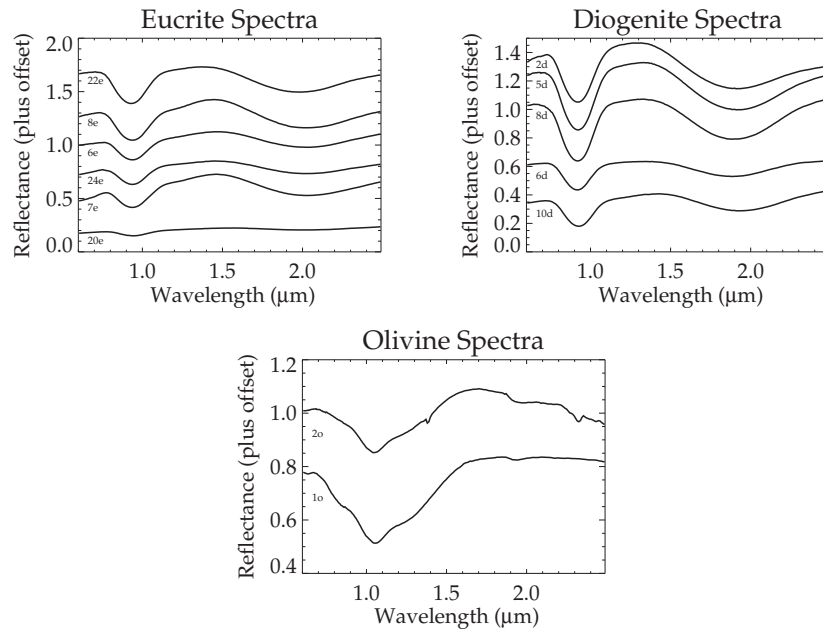
In Fig. 4, we show the frequency of the endmembers found in the case of a linear combination of two endmembers. Eucrite appears to be the most abundant component (68% of the total components), followed by diogenite (25%) and olivine (7%). Taking the above discussion into consideration, we select for our analysis: (1) the eucrites Bereba (6e), Bouvante (7e), Cachari (8e), Padvarninkai (20e), Serra de Mage (22e), Y74450 (24e); (2) the diogenites ALH77256 (2d), GRO95555 (5d), Johnstown (6d), Tatahouine (8d) and Y75032 (10d); and (3) two olivine samples, Jackson County (1o) and Green olivine (2o) (see Table 1). In Fig. 3 we plot the selected endmembers.

4. Evaluation and limits of the linear method

Linear spectral unmixing can be a satisfactory approach for evaluating the composition of a surface (e.g., Bioucas-Dias et al., 2012; Combe et al., 2008), even if a surface is a non-linear (intimate) mixture of several mineralogical phases. The linear assumption implies an error in the estimation of the abundances, but permits only a semi-quantitative estimation of the different components. In this regard, we performed two types of tests: (1) We selected different laboratory mixtures of possible Vesta analogues and we applied linear unmixing to the spectra of such mixtures. This exercise provides an idea of the uncertainty in the

Fig. 1. Example of VIR spectrum before (top) and after (bottom) the removal of the slope.

the band center is defined as the location of the reflectance minimum inside the band as measured on a continuum-removed spectrum. Second, the process of continuum normalization removes the influence of albedo from the unmixing process. Albedo is closely tied to the photometric conditions of the observation rather than mineralogy of the surface. To remove the slope, we consider the line between the first point (0.6 μm) and the last point (2.5 μm) of the spectrum, then we divide the spectrum by this line. To be consistent, the slope was removed in the same way from both VIR spectra and the spectral endmembers (see Fig. 1).

2. We selected a sample of 14 laboratory spectra from a larger spectral library. In Section 3.2, we describe in detail the endmembers and the criteria for their selection.

3. We calculate the χ^2 values for all the combinations. We select the best fit spectrum corresponding with the minimum χ^2 value, with a confidence limit of 95%. In Table 2, we report all the χ^2 values of the bright units, associated to the best-fit, with the corresponding values of the correlation coefficient (r).

Following these steps, the algorithm is able to determine automatically the best combination of endmembers that describe the scene, along with their mixing coefficients. We accept only best fits with $\chi^2 < 1$.

3.2. Endmembers selection

Careful choice of endmembers is necessary to obtain consistent results. In our case, we consider as endmembers a number of laboratory spectra, accounting for pure minerals and for HED meteorites that are assumed to be representative of materials that may be present on Vesta's surface.

We select the endmembers from the Reflectance Experiment Laboratory (RELAB) database (http://www.planetary.brown.edu/relabdocs). The endmembers selection includes consideration of the particle size. The supplementary online material from Reddy et al. (2012b) discusses the grain size differences between eucrite

Fig. 2. Spectral parameter plots for the diogenite and eucrite laboratory samples. The gray circles indicate the samples selected for use as endmembers in this study. The numbers refer to the endmember names in Table 1.

Fig. 3. Spectra of the endmembers selected. The text labels refer to the sample names in Table 1 (6e Bereba, 7e Bouvante, 8e Cachari, 20e Padvarninkai, 22e Serra de Mage, 24e Y74450, 2d ALH77256, 5d GRO95555, 6d Johnstown, 8d Tatahouine, 10d Y75032, 1o Jackson cty, 2o Green olivine).

determination of the abundances. (2) We evaluate the stability of the solution for the VIR data by considering the ten cases showing smaller values of χ^2. If for these χ^2 values we find the same endmembers and similar mixing coefficients, then the solution is stable and the results are reliable.

4.1. Test on laboratory mixtures

To perform this test, we use spectra for sets of mixtures available in the RELAB database, and those used in Cloutis et al. (2013) and Serventi et al. (2013). In Table 1 of the supplementary online material (SOM), we list the spectral endmembers of the mixtures, indicating the origin, the particle size and the texture. We selected mixtures with particle sizes similar to those inferred for Vesta.

In particular, we consider mixtures of two and three laboratory spectra:

1. Olivine and orthopyroxene mixtures.
2. Orthopyroxene and plagioclase mixtures.
3. Millbillillie eucrite and Murchison carbonaceous chondrite.
4. Plagioclase, low and high calcium pyroxenes.
5. Olivine, low and high calcium pyroxenes.

In Section 1 of the SOM and in Fig. 5, all the results obtained for the laboratory mixtures are displayed.

We notice that the error in the estimation of the mixing coefficients depends on the number of endmembers in the mixture and on the endmember itself. Generally, for mixtures of two pyroxenes with a third phase (e.g., plagioclase or olivine), we found differences between the true values and the modeled mixing coefficient
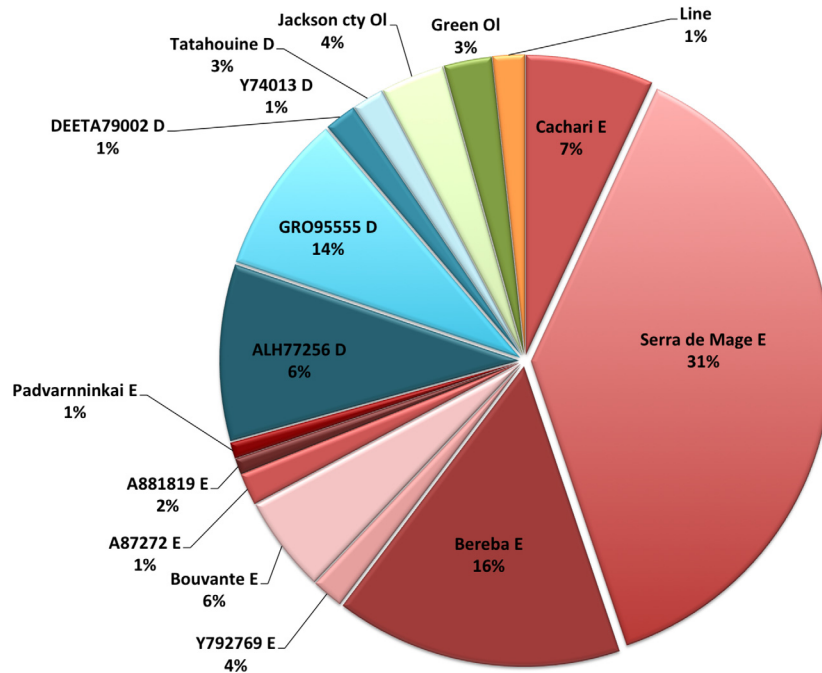
Fig. 4. Frequency of the endmembers for the linear unmixing with two endmembers.

Table 1
Sample name, type, band centers, and band depths for all the endmembers in our spectral library. An identification number is assigned to each spectrum. We chose letter "e" for eucrite, "d" for diogenite, and "o" for olivine.

Endmembers						
Numbers	Name	Type	BCI	BCII	BDI	BDII
1e	A-87272	Eucrite-mmict	0.941	2.002	0.552	0.350
2e	A-881819	Eucrite	0.931	1.966	0.481	0.299
3e	ALH78132	Eucrite-pmict	0.932	1.960	0.426	0.275
4e	ALH85001	Eucrite-Mg rich	0.927	1.946	0.432	0.266
5e	ALHA76005	Eucrite-pmict	0.935	1.980	0.385	0.242
6e	Bereba Bereba	Eucrite-mmict	0.941	2.019	0.419	0.264
7e	Bouvante Bouvante	Eucrite-mmict	0.945	2.009	0.451	0.333
8e	Cachari Cachari	Eucrite-mmict	0.940	2.000	0.543	0.363
9e	EET 87542	Eucrite-br	0.941	2.000	0.254	0.131
10e	EET 90020	Eucrite-unbr	0.941	2.006	0.517	0.276
11e	EETA79005	Eucrite-pmict	0.934	1.970	0.466	0.306
12e	GRO 95533	Eucrite-br	0.941	2.014	0.486	0.330
13e	Ibitira	Eucrite-mmict	0.940	1.994	0.602	0.348
14e	Jonzac	Eucrite-mmict	0.938	2.002	0.542	0.379
15e	Juvinas	Eucrite-mmict	0.936	1.994	0.469	0.298
16e	LEW 87004	Eucrite-pmict	0.935	1.976	0.430	0.261
17e	Millbillillie	Eucrite-mmict	0.938	2.006	0.454	0.273
18e	Moore County	Eucrite-cm	0.938	1.982	0.598	0.378
19e	PCA 82502	Eucrite-unbr	0.941	2.013	0.470	0.338
20e	Padvarninkai	Eucrite-mmict	0.949	2.039	0.232	0.108
21e	Pasamonte	Eucrite-pmict	0.940	2.003	0.494	0.319
22e	SerradeMage	Eucrite-cm	0.931	1.963	0.442	0.286
23e	Stannern	Eucrite-mmict	0.938	2.008	0.405	0.264
24e	Y74450	Eucrite-pmict	0.935	1.985	0.382	0.208
25e	Y792510	Eucrite-mmict	0.942	2.011	0.511	0.324
26e	Y792769	Eucrite-pmict	0.940	2.012	0.408	0.236
1d	A881526	Diogenite	0.919	1.889	0.646	0.428
2d	ALH77256	Diogenite	0.921	1.881	0.588	0.411
3d	Aioun el Atrouss	Diogenite-pm	0.923	1.902	0.631	0.428
4d	EETA79002	Diogenite	0.919	1.877	0.508	0.300
5d	GRO95555	Diogenite-an	0.922	1.908	0.625	0.428
6d	Johnstown	Diogenite	0.917	1.877	0.447	0.247
7d	LAP 91900	Diogenite	0.921	1.903	0.623	0.411
8d	Tatahouine	Diogenite	0.919	1.894	0.633	0.421
9d	Y74013	Diogenite	0.923	1.914	0.422	0.254
10d	Y75032	Diogenite	0.927	1.940	0.517	0.311
1o	Jackson cty	Olivine	1.056	-	0.361	-
2o	Green olivine	Olivine	1.054	-	0.226	-

Table 2

Summary of the results obtained from application of linear spectral unmixing on BM units on Vesta. Endmembers are designated as eucrite ("E"), diogenite ("D"), or olivine ("Ol"), while "Line" refer to the featureless component. Different text color and box color are indicative of variations in composition: Red text refers to eucrite-rich BM units where the featureless endmember (line) is the second most abundant. Yellow text indicates diogenite-rich endmember in which the second most abundant endmember is either the featureless one or olivine. Green text represents cases with olivine as the non-HED spectrum. Red boxes correspond to eucrite-rich BM units with diogenite as the second most abundant endmember. Yellow boxes are diogenite-rich BM units with eucrite as the second most abundant endmember. Green boxes represent the olivine-rich BM units. In the last column are reported the values of the correlation coefficient *r*.

				Linear unmixing results applied to the BM units					
BM unit	Cube	Endm 1	Abundance	Endm 2	Abundance	Endm 3	Abundance	χ^2	r
BU1 RM	(372521396)	Cachari E	0.28	GRO95555 D	0.52	Line	0.20	0.201	0.994
BU2 CWM	(372741836)	Cachari E	0.46	GRO95555 D	0.28	Line	0.26	0.447	0.982
BU2 SM	(372741836)	Cachari E	0.47	Tatahouine D	0.25	Line	0.28	0.342	0.986
BU2 CWM	(395611823)	SerradeMage E	0.86	Jackson cty Ol	0.12	Line	0.02	0.204	0.989
BU2 SM	(395611823)	Cachari E	0.47	Tatahouine D	0.23	Line	0.30	0.247	0.989
BU3 RM	(372385964)	Cachari E	0.32	GRO95555 D	0.46	Line	0.22	0.342	0.989
BU4 CWM	(372212906)	Cachari E	0.41	GRO95555 D	0.45	Line	0.14	0.472	0.987
BU5 CWM	(371993041)	Bouvante E	0.28	GRO95555 D	0.65	Line	0.07	0.705	0.989
BU5 RM	(371993041)	Cachari E	0.20	GRO95555 D	0.57	Line	0.23	0.306	0.990
BU5 SM	(371993041)	Cachari E	0.33	GRO95555 D	0.44	Line	0.23	0.386	0.987
BU6 RM	(372078317)	Cachari E	0.34	GRO95555 D	0.48	Line	0.18	0.312	0.970
BU6 SM	(372078317)	Cachari E	0.44	GRO95555 D	0.44	Line	0.12	0.302	0.992
BU7 RM	(394993455)	Cachari E	0.52	GRO95555 D	0.33	Line	0.15	0.281	0.992
BU8 CWM	(394155284)	Bouvante E	0.24	GRO95555 D	0.65	Line	0.11	0.351	0.991
BU8 SM	(394155284)	Bouvante E	0.23	GRO95555 D	0.61	Line	0.16	0.278	0.977
BU9 CWM	(372430301)	Bouvante E	0.34	Tatahouine D	0.37	Jackson cty Ol	0.29	0.242	0.989
BU9 RM	(372430301)	Cachari E	0.48	Tatahouine D	0.19	Line	0.33	0.229	0.989
BU10 CWM	(371992493)	Cachari E	0.45	GRO95555 D	0.28	Line	0.27	0.296	0.985
BU10 SM	(371992493)	Cachari E	0.51	Tatahouine D	0.22	Line	0.27	0.271	0.988
BU10 CWM	(372609208)	Cachari E	0.44	GRO95555 D	0.28	Line	0.28	0.362	0.973
BU10 SM	(372609208)	Cachari E	0.49	Tatahouine D	0.24	Line	0.27	0.233	0.990
BU11 CWM	(371815732)	Cachari E	0.48	Tatahouine D	0.20	Line	0.32	0.214	0.990
BU11 SM	(372874554)	Cachari E	0.52	Tatahouine D	0.18	Line	0.30	0.280	0.987
BU11 SM	(393801089)	Cachari E	0.53	Tatahouine D	0.18	Line	0.29	0.341	0.985
BU12 CWM	(371632826)	Bouvante E	0.25	GRO95555 D	0.50	Jackson cty Ol	0.25	0.530	0.980
BU12 SM	(371632826)	Bouvante E	0.23	GRO95555 D	0.53	Jackson cty Ol	0.24	0.501	0.982
BU13 SM	(371986649)	Cachari E	0.46	GRO95555 D	0.36	Line	0.18	0.333	0.989
BU14 CWM	(393441792)	Cachari E	0.25	Tatahouine D	0.27	Jackson cty Ol	0.48	0.208	0.988
BU14 SM	(393441792)	Cachari E	0.17	Tatahouine D	0.30	Jackson cty Ol	0.53	0.167	0.989
BU15 CWM	(385962327)	Cachari E	0.32	Tatahouine D	0.56	Line	0.12	0.421	0.989
BU15 SM	(385962327)	Cachari E	0.30	Tatahouine D	0.47	Line	0.23	0.212	0.993
Arruntia CWM	(393750738)	Cachari E	0.29	Tatahouine D	0.23	Jackson cty Ol	0.48	0.269	0.984
Arruntia RM	(393750391)	Bereba E	0.36	Tatahouine D	0.26	Jackson cty Ol	0.38	0.194	0.966
Arruntia SM	(393750738)	Cachari E	0.31	GRO95555 D	0.25	Green Ol	0.44	0.264	0.988
Aelia CWM	(394860977)	Cachari E	0.34	GRO95555 D	0.42	Line	0.24	0.214	0.992
Aelia RM	(394860977)	Cachari E	0.50	Tatahouine D	0.17	Line	0.33	0.260	0.987
Aelia SM	(394860977)	Cachari E	0.09	GRO95555 D	0.67	Line	0.24	0.215	0.993
Bellicia CWM	(393308781)	Cachari E	0.35	Tatahouine D	0.16	Green Ol	0.49	0.490	0.981
Calpurnia CWM	(395166561)	Bouvante E	0.26	Tatahouine D	0.39	Jackson cty Ol	0.35	0.270	0.987
Canuleia CWM	(394198821)	Cachari E	0.45	Tatahouine D	0.39	Line	0.16	0.459	0.983
Canuleia RM	(394198821)	Cachari E	0.44	GRO95555 D	0.46	Line	0.10	0.539	0.987
Canuleia SM	(394198821)	Bouvante E	0.28	Serra de Mage E	0.25	GRO95555 D	0.47	0.632	0.984
Canuleia RM	(394198127)	Cachari E	0.35	GRO95555 D	0.41	Line	0.24	0.353	0.988
Canuleia RM	(371905283)	Cachari E	0.60	GRO95555 D	0.31	Line	0.09	0.577	0.985
Cornelia CWM	(371813008)	Bouvante E	0.28	GRO95555 D	0.58	Jackson cty Ol	0.14	0.381	0.989
Cornelia CWM	(394683501)	Cachari E	0.36	GRO95555 D	0.47	Line	0.17	0.157	0.995
Cornelia SM	(394683501)	Cachari E	0.35	GRO95555 D	0.45	Line	0.20	0.145	0.995
Cornelia CWM	(373313780)	Bouvante E	0.31	GRO95555 D	0.57	Jackson cty Ol	0.12	0.485	0.986
Cornelia SM	(373313780)	Bouvante E	0.25	GRO95555 D	0.59	Jackson cty Ol	0.16	0.315	0.991
Drusilla CWM	(393931377)	Bouvante E	0.28	GRO95555 D	0.55	Jackson cty Ol	0.17	0.420	0.987
Drusilla SM	(393931377)	Bouvante E	0.37	Tatahouine D	0.46	Jackson cty Ol	0.17	0.368	0.987
Eumachia CWM	(394859589)	Cachari E	0.57	Tatahouine D	0.14	Line	0.29	0.342	0.985
Eumachia SM	(394859589)	Cachari E	0.54	Tatahouine D	0.17	Line	0.29	0.328	0.985

Table 2 (continued)

Justina CWM	(372520864)	Cachari E	0.54	Tatahouine D	0.28	Line	0.18	0.296	0.991
Justina RM	(372520864)	Cachari E	0.38	GRO95555 D	0.43	Line	0.19	0.264	0.989
Justina SM	(372520864)	Cachari E	0.42	GRO95555 D	0.35	Line	0.23	0.305	0.989
Justina CWM	(371904187)	Cachari E	0.58	Tatahouine D	0.27	Line	0.15	0.370	0.983
Justina RM	(371904187)	Cachari E	0.41	GRO95555 D	0.44	Line	0.15	0.323	0.992
Justina SM	(371904187)	Cachari E	0.54	Tatahouine D	0.29	Line	0.17	0.335	0.989
Lepida SM	(395256929)	Cachari E	0.45	ALHA77256 D	0.30	Line	0.25	0.595	0.977
Licinia CWM	(395387692)	Bouvante E	0.18	GRO95555 D	0.63	Jackson cty Ol	0.19	0.273	0.992
Licinia SM	(395387692)	Cachari E	0.30	GRO95555 D	0.53	Line	0.17	0.192	0.994
Marcia CWM	(395301166)	Cachari E	0.53	GRO95555 D	0.23	Line	0.24	0.410	0.984
Marcia SM	(395301166)	Cachari E	0.46	GRO95555 D	0.31	Line	0.23	0.396	0.986
Marcia CWM	(395301549)	Cachari E	0.48	GRO95555 D	0.32	Line	0.20	0.301	0.990
Marcia SM	(395301549)	Cachari E	0.48	GRO95555 D	0.30	Line	0.22	0.353	0.987
Myia RM	(372300571)	Cachari E	0.38	GRO95555 D	0.41	Line	0.21	0.396	0.987
Oppia CWM	(373136361)	Bouvante E	0.38	Tatahouine D	0.43	Jackson cty Ol	0.19	0.364	0.986
Oppia SM	(373136361)	Cachari E	0.45	GRO95555 D	0.27	Line	0.28	0.309	0.979
Pinaria CWM	(371727131)	Cachari E	0.41	ALHA77256 D	0.46	Line	0.13	0.332	0.990
Pinaria SM	(371727131)	Bouvante E	0.27	GRO95555 D	0.54	Jackson cty Ol	0.19	0.308	0.990
Sextilia CWM	(371816828)	Cachari E	0.48	GRO95555 D	0.35	Line	0.17	0.461	0.986
Sextilia SM	(371816828)	Cachari E	0.48	GRO95555 D	0.36	Line	0.16	0.484	0.986
Tuccia RM	(372565807)	Cachari E	0.59	Tatahouine D	0.27	Line	0.14	0.319	0.990

up to 11% for the non-pyroxene endmember. In particular, for the case in which the third component is plagioclase, we have an underestimation of this phase of as much as 11% if its abundance is > 50%. In mixtures with plagioclase contents < 40%, the error is lower (Table 2 and Fig. 1 of the SOM). If olivine is one of the endmembers, the difference between the measured abundances and the modeled mixing coefficients is about +10%, when the olivine abundance is ~70%. For lower proportions of olivine in the mixture, the differences between measured and modeled values are decreased (Table 3 and Fig. 2 of SOM and Fig. 5).

For mixtures of just two minerals, the results are similar for low calcium pyroxenes and olivine. The estimated error increases with greater amounts of olivine. In the case of an olivine content of 90%, we found the underestimation of olivine to be 15% (Table 4 and Fig. 3 of the SOM). For lesser proportions of olivine, the error is below 8%. For plagioclase mixed with orthopyroxene at ratios ranging from 90:10 to 20:80, we find a consistent underestimation of plagioclase from 12% to 19% (Table 5 and Fig. 4 of the SOM).

Two-component mixtures of Murchison CC with Millbillillie eucrite have a completely different trend. For Murchison abundances from 5% to 50%, the mixing model consistently overestimated the CC component. The error in CC abundance ranges from 11% to 26% despite the low χ^2 values (Table 6 and Fig. 5 of the SOM). We consider good model results to be those for which the difference between measured and modeled values is 5% (absolute) or less, and we deem results to be acceptable when the difference is < 10% . Cases for which the difference between measured and the modeled values is over 10% were rejected. Our tests on laboratory mixtures reveal that some mixtures can be modeled successfully with the linear method, while some other mixtures may not. Mixtures of different pyroxenes and mixture of pyroxenes with olivine allow a good estimation of the mixing coefficients with the linear methods with respect to the other types of mixtures. In the case of Vesta, we can spectrally model its surface as a mixture of at most three endmembers: pyroxenes, olivine, and a featureless component.

As mentioned previously, our analysis does not consider the absolute reflectance, thus we cannot distinguish high- and low-reflectance featureless phases, but rather the presence of a generic featureless component that weakens and modifies the bands. In the case of plagioclase, we find that the error on plagioclase mixing coefficient decreases with increasing number of endmembers. Unfortunately laboratory data for mixtures of two pyroxenes with CC are not available.

4.2. Stability of the method

To test the stability of the method we consider the results of the 10 models showing the smaller χ^2 values. The method can be considered stable if, for small χ^2 variations, the results do not vary substantially. If small χ^2 variations lead to different endmembers, then the model results cannot be considered to be reliable. In Fig. 6 we plot the best-fit spectrum for the 10 Aelia-SM cases with the lowest χ^2. Variations in χ^2 of the order of 0.0001 led to variations of 1% in the abundances estimation, while the endmembers remain unchanged, indicating robust results. We performed this test on all the VIR spectra under consideration, and we obtained similar results. We thus can conclude that our method yields stable solutions for the choice of the endmembers and the estimation of the mixing coefficients.

5. Bright material units: Lithological variation as revealed by linear unmixing

A first statistical analysis of the BM units on Vesta indicates that the algorithm always chooses three endmembers, and two of these are generally eucrite and diogenite, with comparable frequency (~33%) (Fig. 7). The third endmember is the featureless one with a frequency of 24.8%, while olivine is present in few BM units with a frequency of 8.6% (Fig. 7).

Plots in Fig. 8 show a dependence between the modeled mixing coefficients for eucrite and diogenite found here and the Zambon et al. (2014) band centers for the BM units. We find that the content of eucrite increases with increasing values of band centers, while the content of diogenite increases with decreasing values of band centers. We observe a better correlation between the band II center and eucrite and diogenite mixing coefficient, than for the band I center. Generally, the band I center has a lower variability with respect to the band II center (see Ammannito et al., 2013a; De Sanctis et al., 2012a; Zambon et al., 2015). The poorer correlation between the band I center and the eucrite and diogenite
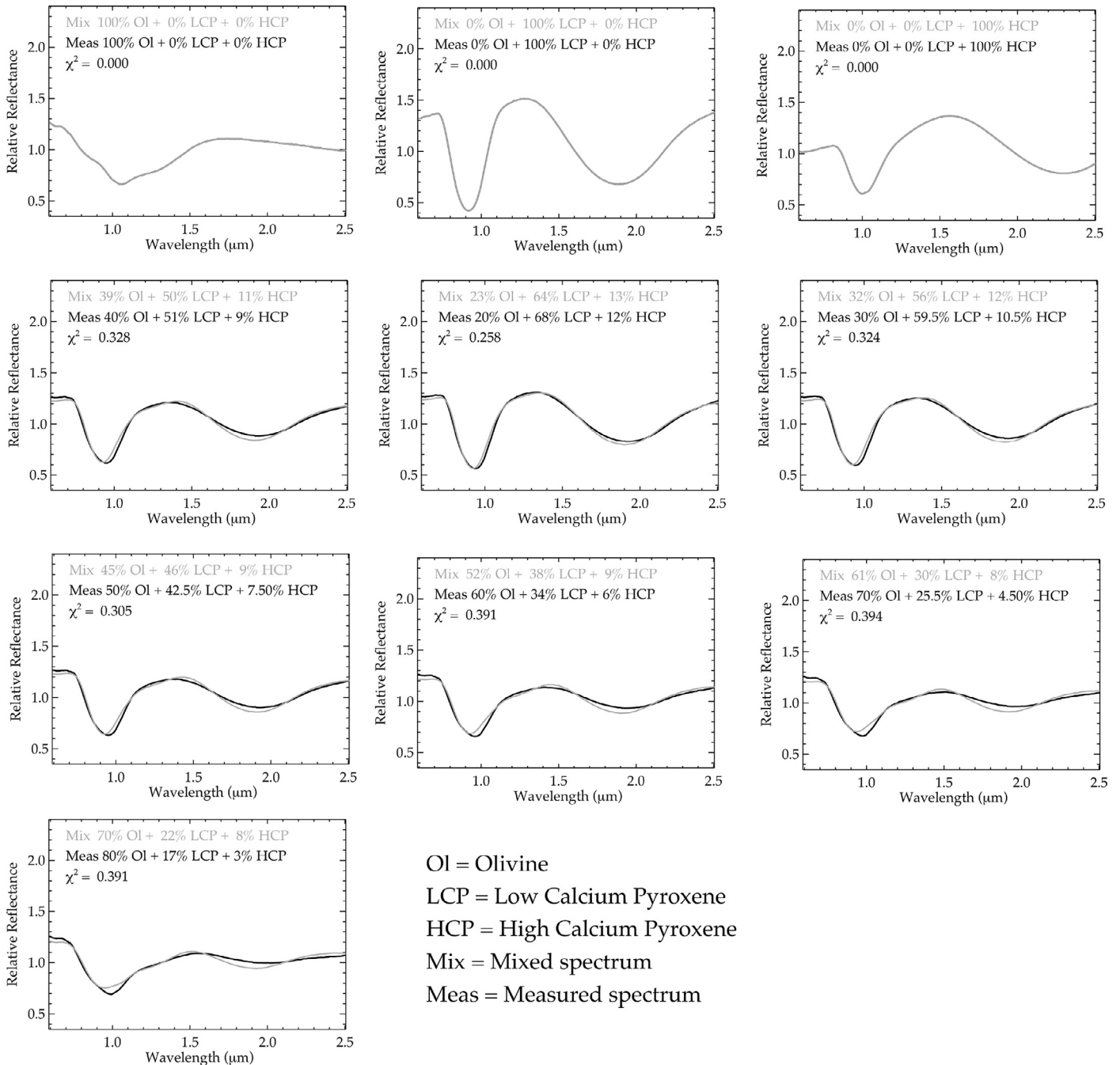
Fig. 5. Linear unmixing applied to a mixture of olivine with low and high calcium pyroxene. The band centers of the modeled spectra are shifted slightly with respect to those of the laboratory spectra. In cases where the χ^2 values differ from 0, there is an imperfect match between the measured and modeled spectra.

mixing coefficients is mainly due to VIR instrumental problems in the vicinity of band I, and on the bridging of the visible and infrared channels. Thus we observe a better correlation between mixing coefficients of eucrite and diogenite and the band II center than for the band I center.

In Fig. 9, we show the linear unmixing application for some representative case of BM units. All the results have been reported in Table 2 and Section 2 of the SOM.

Aelia is a small crater (4.34 km) located at 14.26°S 140.6°E. It is characterized by mixed dark and bright material in its ejecta and by a high diogenite content in its bright slope material (Palomba et al., 2014; Zambon et al., 2014). Linear unmixing results indicate high mixing coefficient of diogenite (67%) for the Aelia-SM

and only 9% of eucrite as expected. Aelia-RM which represents the ejecta showing a greater amount of eucrite than diogenite and a particularly large amount of the featureless endmember (33%). The lower reflectance values of this BM unit suggest the presence of a dark phase that is responsible for reducing the band depths (Fig. 9). Another diogenitic unit is Licinia-SM (Zambon et al., 2014), with mixing coefficients of diogenite (53%) higher than eucrite (30%) (Fig. 9). The bright units with shorter band centers are BU5-CWM and BU5-RM (Zambon et al., 2014), for these BM units we find a diogenite content of 65% and 57% respectively (Fig. 7 of the SOM) and BU8-CWM with a diogenite mixing coefficient of 65% (Fig. 8 of the SOM). Consistent with the findings of Zambon et al. (2014), the most eucritic BM units are Eumachia-CMW with an
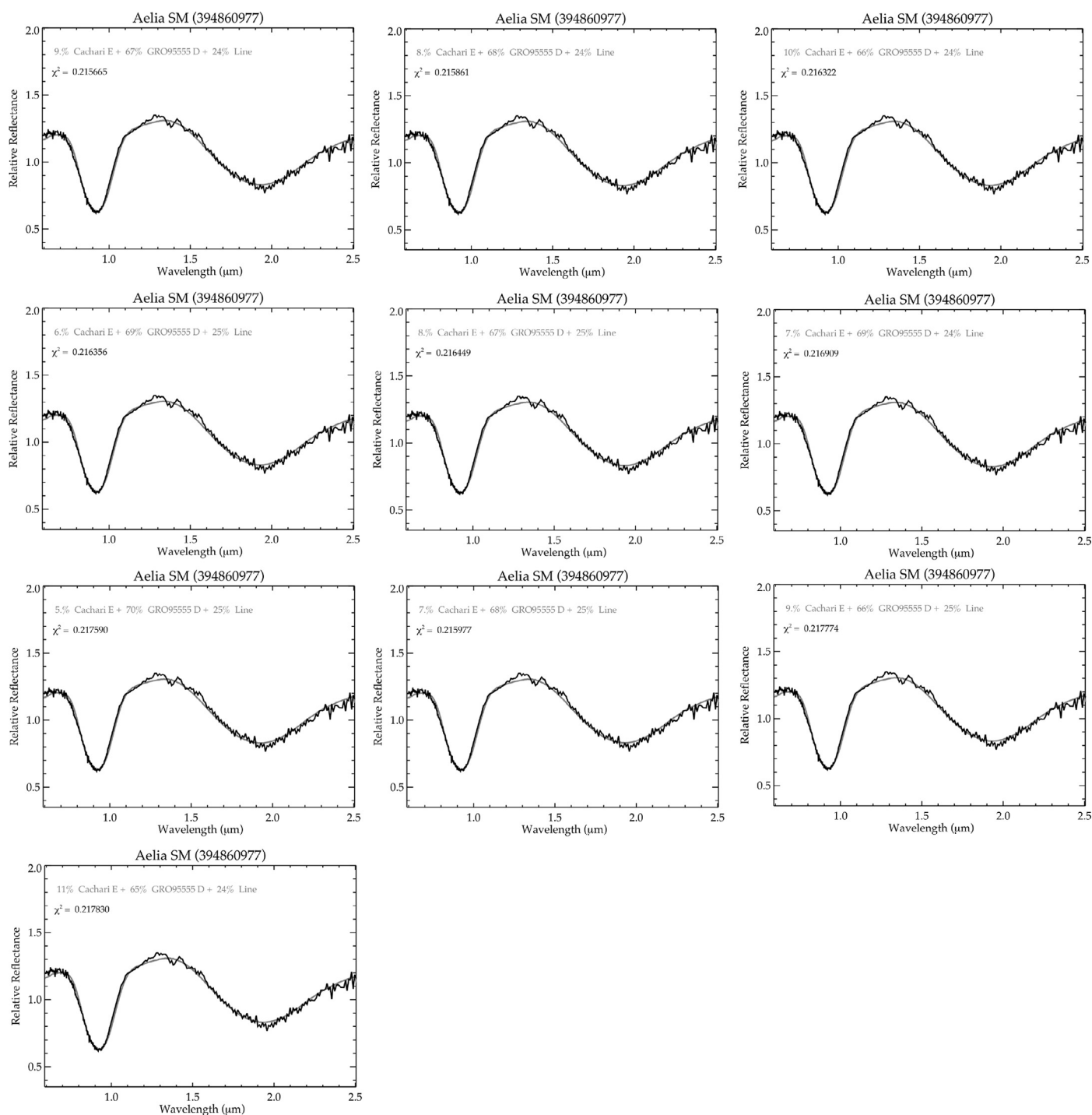
Fig. 6. The results of linear unmixing applied to the Aelia BM unit for the 10 cases with the lowest χ^2. These results indicate that small variations in χ^2 do not correlate with changes in the endmembers or with large variations in the mixing coefficients of the endmembers, attesting to the stability of the results. Black lines are the measured spectra, the gray lines are the model mixture spectra.

eucrite mixing coefficient of 57% and a corresponding diogenite content of 14% of diogenite (Fig. 9), and Tuccia-RM with 57% of eucrite and 27% of diogenite (Fig. 14 of the SOM).

Olivine on Vesta has been identified in few areas, most notably in the region of Bellicia and Arruntia craters, but smaller olivine amounts have been found also near the Albana and Pomponia craters, also located in the northern hemisphere (Palomba et al., 2015). Local olivine enrichments have been suggested by Ruesch et al. (2014) to be present also in the equatorial region and in the southern hemisphere. Our analysis suggests that olivine is present in several BM units, with amounts between 12 and 53%. We iden-

tify sites with large olivine mixing coefficients (>48%) in correspondence with Arruntia, Bellicia in agreement with Ammannito et al. (2013b), and BU14 indicated as detection 3 reported by Ruesch et al. (2014). In these spectra we observe a band I asymmetry typical of olivine and a reduction in the depth of band II, indicating a relatively high amount of olivine, but not high enough to completely obscure band II (Fig. 7). Among the possible olivine-bearing sites found by Ruesch et al. (2014), we note that the Licinia-SM BM unit has a mixing coefficient of olivine as high as 19%. Our algorithm chooses olivine as a third endmember also for regions different from those observed by Ammannito et al. (2013b)
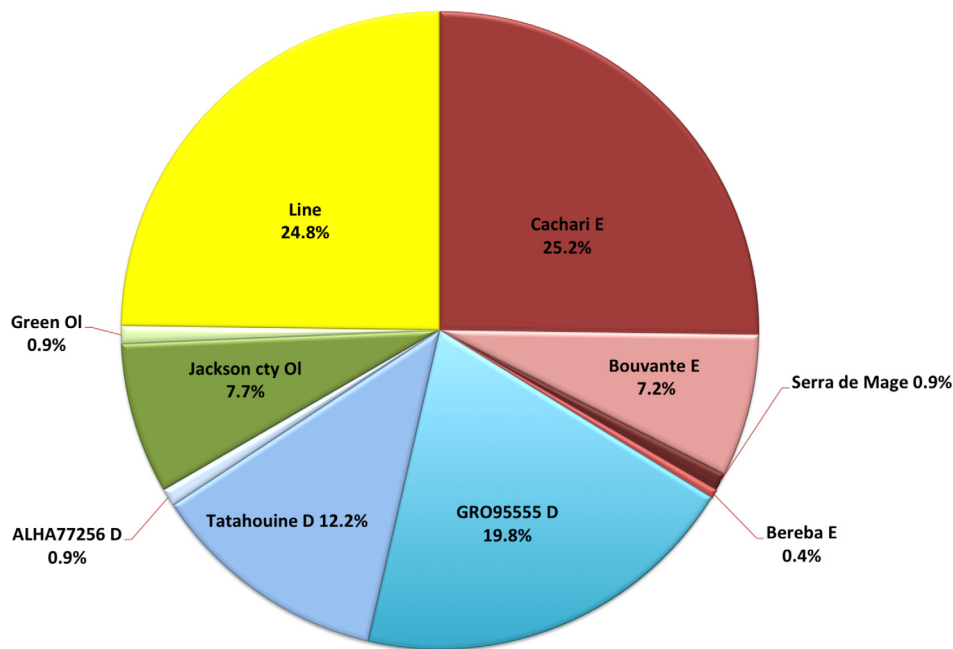
Fig. 7. Frequency of the endmembers selected for the linear unmixing with three endmembers.
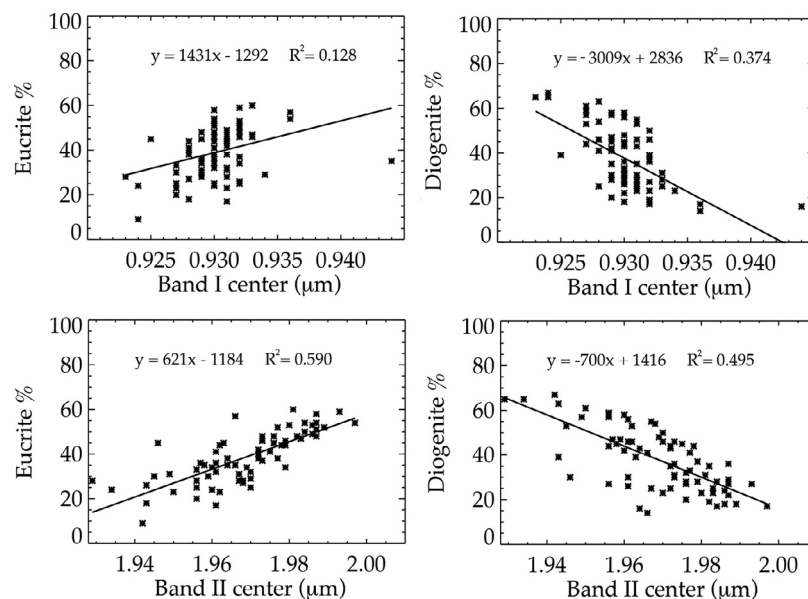

Fig. 8. Plots of band centers vs. eucrite mixing coefficients show that eucrite content increases for increasing band center values. Right: Similar plots for band centers and diogenite mixing coefficients indicate that diogenite content decreases with increasing band center values. Band center values for the BM units are those calculated in Zambon et al. (2014). The coefficient of determination (i.e., the squared correlation coefficient R^2) is also provided.

and Ruesch et al. (2014). Generally we find an olivine mixing coefficient $< 30\%$ for these sites, except for Calpurnia-CWM which has an olivine mixing coefficient of 35% (Fig. 10 of the SOM).

We cannot distinguish between opaque and neutral/featureless high reflectance components. In Fig. 10 we show the relationship between albedo of the BM units (Schröder et al., 2013) and the modeled mixing coefficient of the featureless endmember. In this plot, the albedo tends to decrease with increasing mixing coefficient of the featureless component. We interpret this trend as an indication that the algorithm's selection of the flat endmember can be attributed to the presence of an opaque dark phase in most cases. However, some exceptions exist. The bright streak called BU-15 SM is the brightest unit on Vesta, with a higher content of diogenite (47%) than eucrite (30%). This unit is different from the others because it is characterized by a reduction of the band depth

with respect to the surroundings even though it has high albedo (Zambon et al., 2014). The model composition of BU-15 SM is eucrite and diogenite, with a featureless endmember mixing coefficient of 23% (Table 2). Thus, BU-15 SM may represent a unique case on Vesta, where the presence of a high-albedo featureless component, such as plagioclase, plays an important role in controlling the spectral properties.

6. Discussion

The global compositional analyses hitherto performed on Vesta's surface with Dawn/VIR data were based on the spectral parameters of the kind used by De Sanctis et al. (2012a), and Ammannito et al. (2013b). Spectral parameters are very useful for
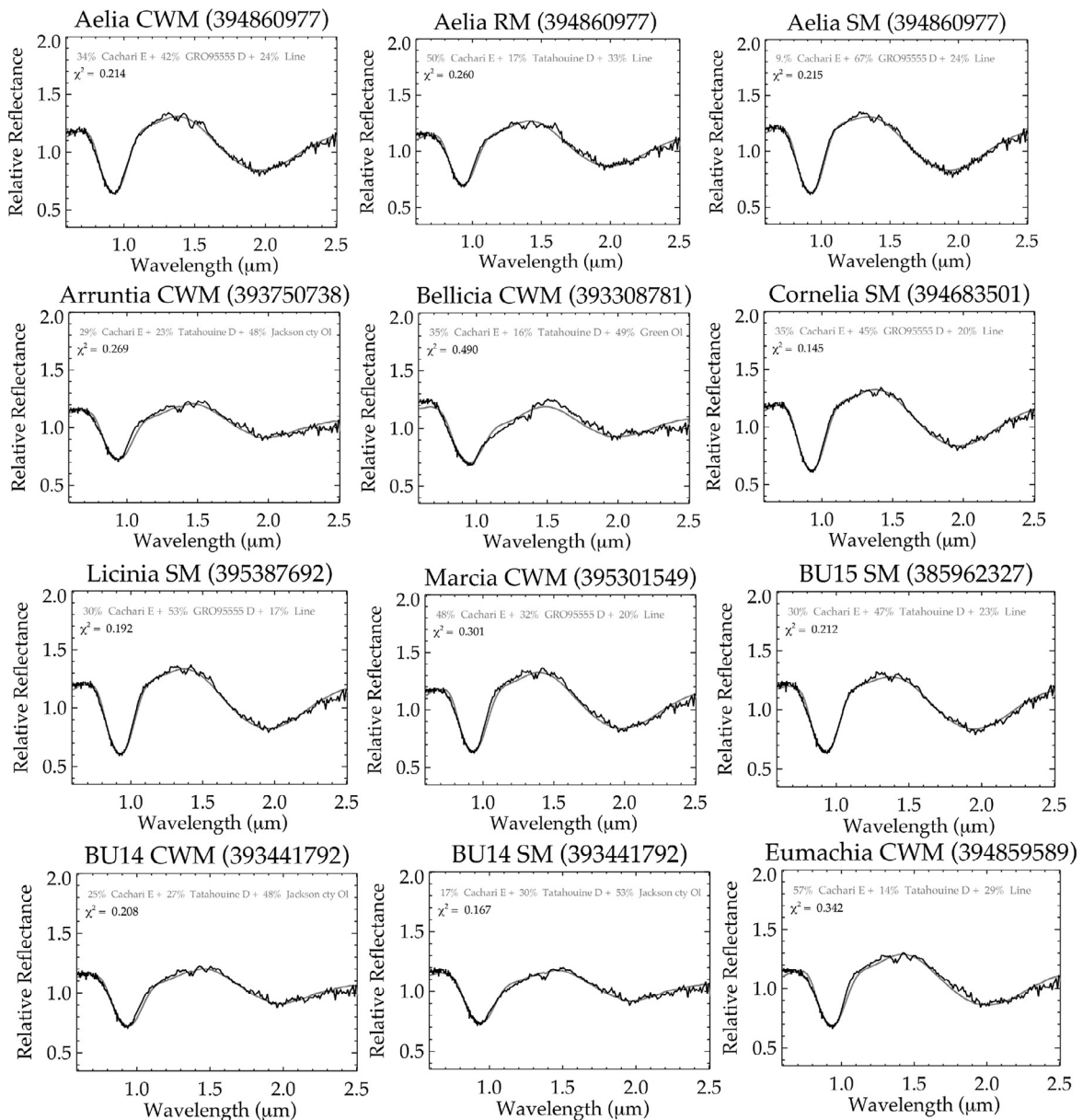
Fig. 9. Examples of linear spectral unmixing applied to BM units. Black lines are the measured spectra, the gray lines are the model mixture spectra. Table 1 summarizes the model endmember mixing coefficients for all the BM units. Related plots are presented in the SOM.

determining the main lithology of a surface, but for a quantitative analysis mixing models are necessary.

In this work, we focused our attention on eucrite and diogenite as the dominant components, plus olivine or a featureless material. We analyzed the Vesta spectra for BM units discussed by Zambon et al. (2014). In that paper, the authors give the results of a compositional analysis based on spectral parameters. Unlike previous papers, the present work determines a semi-quantitative estimation of the mixing coefficients of each lithology. Here we do not consider the spectral slope or the reflectance, and thus we cannot establish the specific nature of this featureless endmember. However, by examining the albedo of each BM unit, we may infer the nature of the featureless phase.

We find that, in general, the mixing coefficient of the featureless endmember is anti-correlated with albedo, suggesting that this component is a low-albedo opaque material. In fact, bright areas are often contaminated by dark material (Jaumann et al., 2012; Palomba et al., 2014). In Fig. 11, we show the main results from

the linear unmixing model plotted on the compositional map from Ammannito et al. (2013b). The mixing coefficients of the different components obtained by the model and the distribution of the BM units are generally in good agreement with previous analyses (e.g., De Sanctis et al., 2012a; 2013b; Zambon et al., 2014). First, in all of the BM units, both eucrite and diogenite spectra are used to fit VIR spectra, reflecting the distribution of those components in the regolith (De Sanctis et al., 2013a, 2013b).

From the results of our analysis, we can see that several BM units are dominated by eucrite and diogenite components (see Section 5 and Table 2). In particular, we can classify these units as eucrite-rich and diogenite-rich units. A third type is olivine-rich BMs.

The distribution of eucrite-rich and diogenite-rich units is similar to the composition of surrounding terrains as inferred by the analysis of spectral parameters.

Olivine-rich BM units are associated with recognized olivine-bearing craters (Ammannito et al., 2013b; Ruesch et al., 2014).
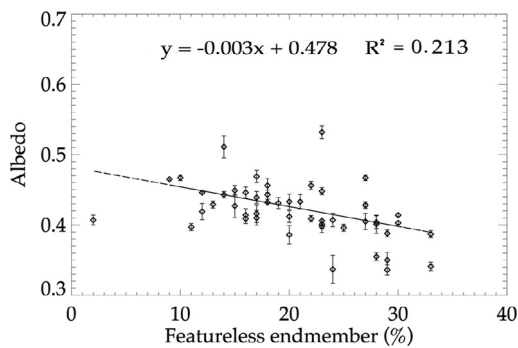
Fig. 10. The albedo of each BM location plotted against the modeled mixing coefficient of the featureless endmember. As albedo decreases, the mixing coefficient of the featureless endmember increases.
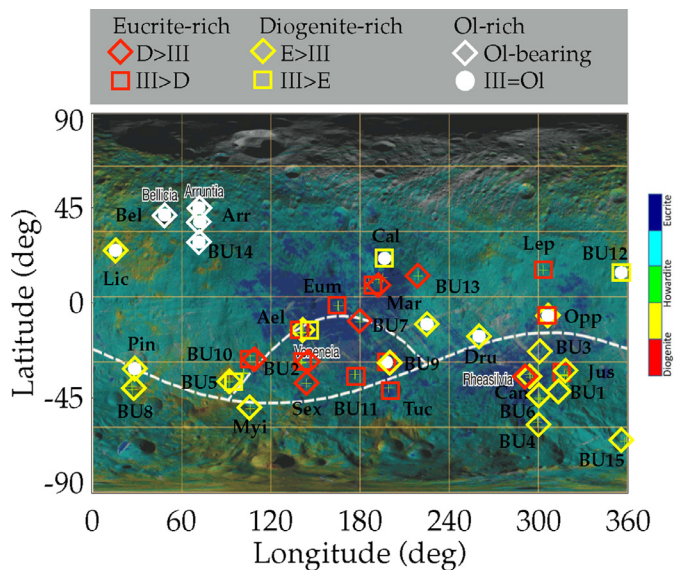
Fig. 11. Results obtained for the linear unmixing applied to BM units overlain on a mineralogical map of Vesta. Red color indicates eucrite-rich units, yellow color designates the diogenite-rich units, and the white symbols are the olivine-rich bright materials. Diamonds indicate BM units for which the eucrite or diogenite mixing coefficient is larger than that of the third endmember. Squares correspond to BM in which the eucrite or diogenite amount is lower than that of the third component. The solid white points are BM units with olivine as the third endmember (see also Table 2). The legend at the top refers to the different cases found in our analysis. For example, "D > III" indicates that the mixing coefficient of the diogenite is greater than those of the third component. "E > III" represents the cases in which the mixing coefficient of the eucrite is greater than that of the third endmember, and so on. (For interpretation of the references to color in this figure legend, the reader is referred to the web version of this article.)

Moreover, where more units are seen in the same crater, they frequently belong to only one family. The only exceptions are a few diogenite-rich units present on eucritic terrains (Aelia, Canuleia, BU3, BU6), and few craters (Aelia, Canuleia, Oppia, Justina, BU9) where BMs show both compositions in the same location.

Eucrite-rich BM units may have a mixing coefficient of eucrite as high as 44% (red symbols in Fig. 11). Those BM units are mostly located in the equatorial region, between 90°E and 300°E longitude, and their distribution is compatible with eucrite-rich regions (Ammannito et al., 2013a). Furthermore, they can be subdivided in two populations: (1) one where the mixing coefficient of diogenite is higher than the mixing coefficient of the featureless endmember (diamond); (2) one where the mixing coefficient of the featureless endmember is greater than the mixing coefficient of diogenite (square). Those subgroups are equally distributed in number and by geography.

In eucrite-rich BM units, the olivine component was never used to fit the spectra. This is consistent with the rare appearance of olivine, as secondary mineral, in eucrite meteorites (Mittlefehldt et al., 1998). There is just one exception, the crater wall material in BU2 (BU2 CWM in Table 2), where the BM is fitted by the Serra de Mage eucrite spectrum (86%), with almost negligible contribution from olivine and the featureless endmember. This is also the only unit where both eucrite and diogenite spectra were not selected. Note that the Serra de Mage eucrite shows spectral characteristics very close to howardite spectra. The spectra of this eucrite are selected only in one other case: the model for an anomalous diogenite rich-units (Canuleia SM) where only HED spectra were used to model the data.

The diogenite-rich BMs are characterized by the association of the highest mixing coefficient of diogenite spectra (yellow symbols in Fig. 11), with a lower threshold of 40%, except for the crater wall unit in BU9 (37%). The distribution of diogenite-rich BMs is widespread in longitude and in latitude, extending farther to the south than eucrite-rich units. The distribution of diogenite-rich BMs is also consistent with the results of previous works and the spectral parameter maps, and they are generally correlated with diogenitic and howarditic terrains (Ammannito et al., 2013a).

Only two regions show diogenite-rich bright materials, within eucrite terrains, the Aelia unit and the units around 300°E, where are concentrated BU3, BU6, and the Canuleia unit. The diogenite-rich BM units can be differentiated by the presence of the eucrite (diamonds in Fig. 11) or another components (square) as the second spectra in the unmixing solutions. Unlike eucrite-rich BM units, the sub-group with the spectra of eucrites selected as the second component is the most frequent, whereas few units are characterized by a non-HED component selected as the second endmember.

Moreover, in various cases (~8.6%) olivine was used instead of the featureless component (white points within diogenite-rich BMs), even if with mixing coefficient lower than 30%, with the exception of the crater wall unit in Calpurnia (35%). Aelia and Canuleia craters are both in eucritic terrains and they show both eucrite-rich and diogenite-rich BM locations. Aelia has diogenite-rich type-1 BMs on the wall, whereas the radial material (RM) is eucrite-rich. This could indicate that the Aelia impact exposed diogenite blocks from greater depths, whereas fresh eucritic material that originally resided close to or at the surface was ejected to form the radial material. In Canuleia we have both type-1 and type-2 BMs with eucrite and diogenite, whose difference is less than 64%, indicating a balanced distribution of these spectral endmembers, i.e., a howarditic composition.

Only one Aelia BM unit, the RM, shows a clear eucrite-rich composition.

In contrast, BU3 and BU6 craters show both diogenite-rich units as RM (BU6 has also the SM, see Table 2). Those units are very close to the diogenite terrains, so perhaps the presence of diogenite-rich material can be attributed to contributions from southern craters. Alternately, it could be that the eucritic crust in that area is thinner, and thus fresh diogenitic material was more easily excavated and ejected from those craters.

Three other craters (Oppia, BU9 crater, and Justina) show the presence of both eucrite- and diogenite-rich BMs. In the Oppia crater, two BM units are on the wall. The CWM are diogenite-enriched, whereas the corresponding slope material (SM) is characterized by a higher amount of eucrite. In the second crater (BU9), the CWM is diogenite-rich, whereas the RM BM unit is fitted by a high mixing coefficient of eucrite. BM units at crater Justina have been covered by VIR more than one time, the four wall units (both CWM and SM) are eucrite-rich and the two RM are diogenite-rich BM units. A third family is made of olivine-rich bright units, i.e., where olivine spectra are selected as the most

abundant component. In this family, all of the recognized BMs are enriched in olivine, with diogenite > eucrite in BU14 and eucrite > diogenite in Arruntia and Bellicia areas. These proportions are in agreement with those found by analysis of spectral parameters in Zambon et al. (2014). These units are located in the northern hemisphere and correspond to the olivine-bearing sites detected by Ammannito et al. (2013b) and Ruesch et al. (2014). For Bellicia and BU14, we find an olivine mixing coefficient around of ∼50%, with slightly lower values found in Arruntia. These values indicate that olivine is a dominant component in these sites (Ammannito et al., 2013b).

High abundances of olivine are generally expected to be present in mantle and plutonic rocks, which could be present in topographically low areas. In this work, we have employed Mg-rich olivine endmembers with very fine particle sizes, compatible with the predicted Vesta dominant regolith size. Therefore, the absolute abundance values could be lower than suggested by our models, in particular considering that olivine is more fayalitic (Fe-rich) in HEDs. Olivine that is richer in iron has a stronger absorption band, and hence a lower abundance of such Fe-rich olivine (relative to Mg-rich olivine) would be needed to model a given spectrum.

Poulet et al. (2015) discussed the retrieval of composition from VIR spectra by using a non-linear method (Shkuratov et al., 1999). It should be noted that the results from a non-linear technique, although in principle better than those from a linear model, can suffer if the starting data has not been properly treated. For the VIR dataset, extreme care must be taken, for example, in bridging the sections VIS and IR, exclusion of spectral channels suffering from recurring artifacts, and removal of the continuum. Poulet et al. (2015) concluded that coarse-grained olivine is likely to be present in all major units of Vesta. In general, they also found that the abundance of olivine could be lower because of the presence of iron-rich olivine or because of an increase in the grain size of olivine with respect to the other phases. An alternative hypothesis that could explain higher surface abundances of olivine in such northern locations is an exogenic origin—e.g., material delivered by an olivine-rich impactor, as suggested by Le Corre et al. (2015). Moreover, we find that in those terrains the third selected endmember is frequently a featureless component.

As discussed above, the mixing coefficient of the featureless endmember is anti-correlated with the albedo, suggesting that this component is associated with low-albedo CC-like opaque material. In fact, bright areas are often contaminated by dark material (Jaumann et al., 2012; Palomba et al., 2014). We do find one exception where a BM unit with a large mixing coefficient for the featureless endmember, BU15-SM, has the highest albedo (Zambon et al., 2014). This unit is matched by a diogenite-rich bright unit extending into the Rheasilvia basin, and Zambon et al. (2014) predicted the possible presence of a bright component.

The major bright, iron-poor, mineral in HEDs and in basic igneous composition is plagioclase, which can have a large abundance in magmatic rocks, both effusive and cumulitic, intrusive rocks. Plagioclase can exhibit a characteristic absorption at 1.25μm caused by impurity iron at abundances corresponding to FeO < 1% (e.g. Burns, 1993; Cheek et al., 2011; Serventi et al., 2013), However, the 1.25μm feature cannot be recognized in mixtures with mafic iron-bearing silicates unless the plagioclase is present in very large amounts. If plagioclase is indeed revealed by our analysis, it should be noted that in HEDs it is generally present in eucrites and cumulitic eucrites, but not in diogenites.

Another important aspect showed by our results is the selection of olivine spectra with low mixing coefficient for the diogenite-rich BM units, in place of the featureless endmember. From a spectroscopic viewpoint, this implies that reductions of the intensities of band I and band II are not correlated, otherwise the model should have selected the featureless spectrum. In addition, a weak asym-

metry around the 1-μm absorption is revealed, so the selection of only eucrite and diogenite spectra alone is not able to properly fit VIR data in that specific spectral region. The presence of this low amount of olivine in the diogenite-rich BM units indicates that iron could be present in one or more phases with a band around 1 μm but with a very weak, or absent, absorption around 2 μm. In general, these spectral characteristics are consistent with the presence of olivine, high-Ca pyroxene, plagioclase or a glassy component, in basic igneous compositions.

Iron-bearing silicate glasses (e.g., volcanic or impact glasses) have a dominant crystal-field absorption at ∼ 1.1μm, the intensity of which depends on the iron abundance. Thus a glassy component cannot be excluded in units that are formed by impacts. In fact, impact melts have been identified in some HEDs (see e.g., Metzler and Stoffler, 1995; Singerling et al., 2013). High-Ca pyroxenes are not abundant in diogenites, even if there are samples where they are found in abundance higher than 10% (e.g., Mittlefehldt et al., 1998). High-Ca pyroxene can also be frequently found as exolution lamellae in orthopyroxene crystals, influencing the spectral characteristics of the host low-Ca hosting pyroxene (Gaffey et al., 2002).

Olivine is difficult to detect, especially in small amounts. The shape and the position of the 1μm band are influenced by the presence of olivine if it is present in high amounts in mixtures with pyroxene (e.g. in particular the orthopyroxene–olivine mixtures studied by Beck et al., 2013; Cloutis et al., 1986).

Beck et al. (2013) argued that olivine could be recognized only at contents > 30% in HEDs, because under this threshold, the olivine is masked in mixtures with orthopyroxene. Beck et al. (2013) predicted that olivine in diogenite and harzburgite terrains could not be detected when present in amounts below this threshold. Recent studies by Horgan et al. (2014) and Shestopalov et al. (2015) suggest two different methods for detection of small amounts of olivine in mixtures with pyroxene. Horgan et al. (2014) used different spectral indices to identify the presence of olivine in the spectra of Mars. Shestopalov et al. (2015) observed that the uncertainty (variance) of the band center position in spectra of laboratory olivine-pyroxene mixtures depends on the shift of the band center at 950 nm. They found that mixtures with different olivine contents can be identified by their position in a plot of the variance vs. band center at 950 nm.

On the other hand, Poulet et al. (2015) concluded that best fits to all the studied Vesta terrains are achieved when a component of forsteritic olivine (Fo70) is included. They also emphasized that the particle size has an effect on the olivine abundance obtained by a non-linear unmixing method. Olivine-rich melts were recently found in some howardites (Beck et al., 2013), so we cannot rule out that those BM units could have low olivine mixing coefficient.

7. Conclusions

1. To model VIR data for Vesta, we applied a linear spectral unmixing model. Our analysis does not take into account the spectral slope and the albedo but only the spectral shape.
2. Tests on laboratory mixtures of olivine and low- and high-calcium pyroxene indicate that olivine mixing coefficients are underestimated with an accuracy within 10% for olivine amounts > 50%. For mixtures of plagioclase with low-and high-calcium pyroxenes, the plagioclase amount is underestimated within 11% for plagioclase contents > 40%. Analysis of mixtures of Millbillillie eucrite with carbonaceous chondrite (CC) material indicates that the CC abundance was overestimated by up to 26%.
3. Linear unmixing applied to Vesta spectra is able to detect the principal HED and non-HED lithologies present on the asteroid.

4. We can divide the bright material units into three main groups: eucrite-rich, diogenite-rich, and olivine-rich, depending on the most abundant endmember used to fit the spectrum. The non-HED endmember can be either olivine or a featureless component. This confirms that Vesta is composed of a high content of pyroxenes mixed with a lower concentration of other mineralogical phases.

5. The third endmember is often the featureless phase, which is associated with a reduction in the strength of both pyroxene bands. The mixing coefficient of the featureless endmember is anticorrelated with albedo, suggesting that the featureless phase can be associated with low-albedo, CC-like opaque material.

6. Large amounts of olivine are detected in the Bellicia, Arruntia and BU14 BM units. Where lower olivine contents ($<30\%$) are found, the sites are generally associated with high concentrations of diogenite.

Acknowledgments

Supplementary material

Supplementary material associated with this article can be found, in the online version, at 10.1016/j.icarus.2016.01.009.

References

Adams, J.B., Smith, D.E., Johnson, T.V., 1986. Spectral mixture modeling: A new analysis of rock and soil types at the Viking Lander 1 site. Journal of Geophysical Research 91, 8098–8112.

Ammannito, E., De Sanctis, M.C., Capaccioni, F., et al., 2013a. Vestan lithologies mapped by the Visual and InfraRed spectrometer on Dawn. Meteoritics and Planetary Science 48 (11), 2185–2198.

Ammannito, E., De Sanctis, M.C., Palomba, E., et al., 2013b. Olivine from Vesta's mantle exposed on the surface. Nature 504, 122–125.

Beck, A.W., McCoy, T.J., Sunshine, J.M., et al., 2013. Challenges in detecting olivine on the surface of 4 Vesta. Meteoritics and Planetary Science 48 (11), 2155–2165.

Beck, A.W., McSween, H.Y., 2010. Diogenites as polymict breccias composed of orthopyroxenite and harzburgite. Meteoritics and Planetary Science 45, 850–872.

Beck, A.W., McSween, H.Y., Viviano, C.E., 2011. Petrologic and textural diversity in one of the largest samples of the vestan regolith. In: 74th Annual Meeting of the Meteoritical Society, p. A16.

Binzel, R.P., Gaffey, M.J., Thomas, P.C., et al., 1997. Geologic mapping of Vesta from 1994 Hubble Space Telescope images. Icarus 128, 95–103.

Bioucas-Dias, J.M., Plaza, A., Dobigeon, N., et al., 2012. Hyperspectral unmixing overview: Geometrical, statistical, and sparse regression-based approaches. IEEE Journal of Selected Topics in Applied Earth Observations and Remote Sensing 5, 354–379.

Blewett, D.T., Hawke, B., Lucey, P.G., et al., 1995. Remote sensing and geologic studies of the Schiller-Schickard region of the Moon. Journal of Geophysical Research 100 (E8), 16959–16978.

Bobrovnikoff, N.T., 1929. The spectra of minor planets. Lick Observatory Bulletin 407, 18–27.

Burbine, T.H., Buchanan, P.C., Dolkar, T., et al., 2009. Pyroxene mineralogies of near-Earth vestoids. Meteoritics and Planetary Science 44, 1331–1341.

Burns, R., 1993. Mineralogical Applications of Crystal Field Theory, second ed. Cambridge University Press.

Cheek, L.C., Pieters, C.M., Boardman, J.W., et al., 2011. Goldschmidt crater and the Moon's north polar region: Results from the Moon mineralogy mapper (m3). Journal of Geophysical Research 116 (E00G02), 1–15. doi:10.1029/2010JE003702.

Clark, R.N., 1999, vol. 3. Remote Sensing for the Earth Sciences—Manual of Remote Sensing. John Wiley and Sons, New York.

Cloutis, E.A., Gaffey, M.J., Jackowski, T.L., et al., 1986. Calibrations of phase abundance, composition, and particle size distribution for olivine-orthopyroxene mixtures from reflectance spectra. Journal of Geophysical Research 91, 641–653.

Cloutis, E.A., Izawa, M.R.M., Pompilio, L., et al., 2013. Spectral reflectance properties of HED meteorites + CM2 carbonaceous chondrites: Comparison to HED grain size and compositional variations and implications for the nature of low-albedo features on Asteroid 4 Vesta. Icarus 223, 850–877.

Combe, J.-P., Le Moulic, S., Sotin, C., et al., 2008. Analysis of OMEGA/Mars Express data hyperspectral data using a multiple-endmember linear spectral unmixing model (MELSUM): Methodology and first results. Planetary and Space Science 56 (7), 951–975.

Consolmagno, G.J., Drake, M.J., 1977. Composition and evolution of the eucrite parent body—Evidence from rare Earth elements. Geochimica et Cosmochimica Acta 41, 1271–1282.

Dalton, J.B.I., 2007. Linear mixture modeling of Europa's non-ice material based on cryogenic laboratory spectroscopy. Geophysical Research Letters 34 (L21205), 1–4. doi:10.1029/2007GL031497.

Dalton, J.B.I., Shirley, J.H., Cassidy, T., et al., 2011. Spectral properties of hydrated sulfate minerals on Mars. In: Vol. 6, EPSC-DPS2011-650, 2011.

De Sanctis, M., Ammannito, E., Capria, M., et al., 2012a. Spectroscopic characterization of mineralogy and its diversity across Vesta. Science 336, 697–700.

De Sanctis, M., Ammannito, E., Palomba, E., et al., 2013a. Possible detection of olivine on Vesta. In: 44th LPSC.

De Sanctis, M., Coradini, A., Ammannito, E., et al., 2011. The VIR spectrometer. Space Science Reviews 163, 329–369.

De Sanctis, M.C., Ammannito, E., Capria, M.T., et al., 2013b. Vesta's mineralogical composition as revealed by the Visible and InfraRed spectrometer on Dawn. Meteoritics and Planetary Science 48 (11), 2166–2184. doi:10.1111/maps.12138.

De Sanctis, M.C., Combe, J.-P., Ammannito, E., et al., 2012b. Detection of widespread hydrated materials on Vesta by the VIR imaging spectrometer on board the DAWN mission. The Astrophysical Journal Letters 758 (2), 1–5. doi:10.1088/2041-8205/758/2/L36. Article ID. L36.

Donaldson Hanna, K., Sprague, A.L., 2009. Vesta and the HED meteorites: Mid-infrared modeling of minerals and their abundances. Meteoritics and Planetary Science 44 (11), 1755–1770.

Feierberg, M.A., Drake, M.J., 1980. The meteorite-asteroid connection—The infrared spectra of eucrites, shergottites, and Vesta. Science 209, 805–807.

Fox III, L., Fischer, A.F., Gillespie, A.R., et al., 1990. Using spectral mixture analysis of AVIRIS high dimensional data for distinguishing soil chronosequences. In: Proceedings of the Airborne Science Workshop: AVIRIS. Jet Propulsion Laboratory.

Gaffey, M.J., Cloutis, E.A., Kelley, M.S., et al., 2002. Mineralogy of Asteroids. Asteroids III. University of Arizona Press, Tucson.

Hapke, B., 1981. Bidirectional reflectance spectroscopy. I—Theory. Journal of Geophysical Research 86, 3039–3054.

Hapke, B., 2012. Theory of reflectance and emittance spectroscopy, 2nd edition. Cambridge University Press.

Hiroi, T., Pieters, C.M., Takeda, H., 1994. Grain size of the surface regolith of asteroid 4 Vesta estimated from its reflectance spectrum in comparison with HED meteorites. Meteoritics 29, 394–396.

Horgan, B.H.N., Cloutis, E.A., Mann, P.J., et al., 2014. Near-infrared spectra of ferrous mineral mixtures and methods for their identification in planetary surface spectra. Icarus 234, 132–154.

Jaumann, R., Williams, D.A., Buczkowski, D., et al., 2012. Vesta's shape and morphology. Science 336 (6082), 687–690.

Keshava, N., Mustard, J., 2002. Spectral unmixing. IEEE Signal Processing Magazine 19 (1), 44–57.

Lawrence, D.J., Peplowski, P.N., Prettyman, T.H., et al., 2013. Constraints on Vesta's elemental composition: Fast neutron measurements by dawn's gamma ray and neutron detector. Meteoritics and Planetary Science 48 (11), 2271–2288.

Le Corre, L., Reddy, V., Sanchez, J.A., et al., 2015. Exploring exogenic sources for the olivine on asteroid (4) Vesta. Icarus 258, 483–499. doi:10.1016/j.icarus.2015.01.018.

Le Corre, L., Reddy, V., Schmedemann, N., et al., 2013. Olivine or impact melt: Nature of the "orange" material on Vesta from Dawn. Icarus 226 (2), 1568–1594.

Li, J.Y., McFadden, L.A., Thomas, P.C., et al., 2010. Photometric mapping of asteroid (4) Vesta's southern hemisphere with hubble space telescope. Icarus 208, 238–251.

Li, J.-Y., Mittlefehldt, D.W., Pieters, C.M., et al., 2012. Investigating the origin of bright materials on Vesta: Synthesis, conclusions, and implications. In: 43rd LPSC, 2012.

Longobardo, A., Palomba, E., Capaccioni, F., et al., 2014. Photometric behavior of spectral parameters in Vesta dark and bright region as inferred by the Dawn VIR spectrometer. Icarus 240, 20–35.

Lupishko, D.F., Bel'Skaia, I.N., Kvaratskheliia, O.I., et al., 1988. The polarimetry of Vesta during the 1986 opposition. Astronomicheskii Vestnik 22, 142–146.

Mayne, R.G., Sunshine, J.M., McSween, H.Y., et al., 2010. Petrologic insights from the spectra of the unbrecciated eucrites: Implications for Vesta and basaltic asteroids. Meteoritics and Planetary Science 45, 1074–1092.

McCord, T.B., Adams, J.B., Johnson, T.V., 1970. Asteroid Vesta: Spectral reflectivity and compositional implications. Science 168, 1445–1447.

McCord, T.B., Li, J.-Y., Combe, J.-P., et al., 2012. Dark material on Vesta from the infall of carbonaceous volatile-rich material. Nature 461, 83–86.

McSween, H.Y., Ammannito, E., Reddy, V., et al., 2013. Composition of the Rheasilvia basin, a window into Vesta's interior. Journal of Geophysical Research 118, 335–346.

McSween, H.Y., Mittlefehldt, D.W., Beck, A.W., et al., 2011. Meteorites and their relationship to the geology of Vesta and the Dawn mission. Space Science Reviews 163, 141–174.

Metzler, K., Stoffler, D., 1995. Impact melt rocks and granulites from the hed asteroid. Meteoritics 30 (5), 547.

Mittlefehldt, D.W., Li, J.-Y., Pieters, C.M., et al., 2012. Types and distribution of bright materials on 4 Vesta. In: 43rd LPSC, 2012.

Mittlefehldt, D.W., McCoy, T.J., Goodrich, C.A., et al., 1998. Non-chondritic meteorites from asteroids bodies. In: Papike, J.J. (Ed.). Planetary Materials, Chapter 4, Mineralogical Society of America, vol. 36.

Palomba, E., Longobardo, A., De Sanctis, M.C., et al., 2014. Composition and mineralogy of dark material deposits on Vesta. Icarus 240, 58–72.

Palomba, E., Longobardo, A., De Sanctis, M.C., et al., 2015. Detection of new olivine-rich locations on Vesta. Icarus 258, 120–134.

Pieters, C.M., Englert, A.J., 1993. Remote Geochemical Analysis: Elemental and Mineralogical Composition. Press Syndicate of University of Cambridge, Cambridge, England.

Poulet, F., Ruesch, O., Langevin, Y., et al., 2015. Modal mineralogy of the surface of Vesta: Evidence for ubiquitous olivine and identification of meteorite analogue. Icarus 253, 354–377.

Prettyman, T.H., Beck, A.W., Feldman, W.C., et al., 2014. Vesta's elemental composition. In: 44rd LPSC, 2013.

Prettyman, T.H., Feldman, W.C., McSween, H.Y., et al., 2011. Dawn's Gamma Ray and Neutron Detector. Space Science Reviews 163, 371–459.

Prettyman, T.H., Mittlefehldt, D.W., Yamashita, N., et al., 2013. Neutron absorption constraints on the composition of 4 Vesta. Meteoritics and Planetary Science 48 (11), 2211–2236.

Ramsey, M.S., Christensen, P.R., 1992. The linear "unmixing" of laboratory thermal infrared spectra: implications for the Thermal Emission Spectrometer (TES) experiment, Mars observer. In: 23rd LPSC, 2013.

Reddy, V., Le Corre, L., O'Brien, D.P., et al., 2012a. Delivery of dark material to Vesta via carbonaceous chondritic impacts. Icarus 223, 544–559.

Reddy, V., Li, J.-Y., Le Corre, L., et al., 2013. Comparing Dawn, Hubble Space Telescope, and ground-based interpretations of (4) Vesta. Icarus 226, 1103–1114.

Reddy, V., Nathues, A., Le Corre, L., et al., 2012b. Color and albedo heterogeneity of Vesta from Dawn. Science 336, 700–704.

Reddy, V., Sanchez, J.A., Nathues, A., et al., 2012c. Photometric, spectral phase and temperature effects on 4 Vesta and HED meteorites: Implications for the Dawn mission. Icarus 217, 153–168.

Roatsch, T., Kersten, E., Matz, K.-D., et al., 2012. High resolution Vesta High Altitude Mapping Orbit (HAMO) Atlas derived from Dawn framing camera images. Planetary and Space Science 73, 283–286.

Ruesch, O., Hiesinger, H., De Sanctis, M.C., et al., 2014. Detections and geologic context of local enrichments in olivine on Vesta with VIR/Dawn data. Journal of Geophysical Research 119 (9), 2078–2108.

Russell, C.T., Raymond, C.A., 2011. The Dawn mission to Vesta and Ceres. Space Science Reviews 163, 3–23.

Russell, C.T., Raymond, C.A., et al., 2012. Dawn at Vesta: Testing the protoplanetary paradigm. Science 336, 684–686.

Schröder, S.E., Mottola, S., Keller, H., 2013. Resolved photometry of Vesta reveals physical properties of Crater Regolith. Planetary and Space Science 85, 198–213. doi:10.1016/j.pss.2013.06.009.

Serventi, G., Carli, C., Sgavetti, M., et al., 2013. Spectral variability of plagioclase–mafic mixtures (1): Effects of chemistry and modal abundance in reflectance spectra of rocks and mineral mixtures. Icarus 226, 282–298.

Shestopalov, D.I., Golubeva, L.F., Cloutis, E.A., 2015. Remote sensing olivine in pyroxene-bearing targets: The case of v-type asteroids. In: 46th LPSC, 2015.

Shestopalov, D.I., McFadden, L.A., Golubeva, L.F., et al., 2010. About mineral composition of geologic units in the northern hemisphere of Vesta. Icarus 209 (2), 575–585.

Shkuratov, Y., Starukhina, L., Hoffmann, H., et al., 1999. A model of spectral albedo of particulate surfaces: Implications for optical properties of the Moon. Icarus 137, 235–246.

Singer, R.B., McCord, T.B., 1979. Mars: Large scale mixing of bright and dark surface materials and implications for analysis of spectral reflectance. In: 10th LPSC, pp. 1835–1848.

Singerling, S.A., McSween, H.Y., Taylor, L.A., 2013. Glasses in howardites: Impact melts or pyroclasts? Meteoritics & Planetary Science 48 (5), 715–729.

Thangjam, G., Reddy, V., Le Corre, L., et al., 2013. Lithologic mapping of HED terrains on Vesta using Dawn Framing Camera color data. Meteoritics and Planetary Science 48 (11), 2199–2210.

Thomas, P.C., Binzel, R.P., Gaffey, M.J., et al., 1997. Impact excavation on Asteroid 4 Vesta: Hubble Space Telescope results. Science 227, 1492–1495.

Tosi, F., Capria, M.T., De Sanctis, M.C., et al., 2014. Thermal measurements of dark and bright surface features on Vesta as derived from Dawn/VIR. Icarus 240, 36–57.

Tosi, F., Frigeri, A., Combe, J.-P., et al., 2015. Mineralogical analysis of the Oppia quadrangle of asteroid (4) Vesta: Evidence for occurrence of moderate-reflectance hydrated minerals. Icarus 259, 129–149.

Williams, D.A., Yingst, R., Garry, W., 2014. Introduction: The geologic mapping of Vesta. Icarus 244, 1–12.

Zambon, F., De Sanctis, M.C., Schröder, S.E., et al., 2014. Spectral analysis of the bright materials on the Asteroid Vesta. Icarus 240, 73–85.

Zambon, F., Frigeri, A., Combe, J.-P., et al., 2015. Spectral analysis of the quadrangles av-13 and av-14 on Vesta. Icarus 259, 181–193.